

Published in final edited form as:

*Int J Comput Assist Radiol Surg.* 2012 November ; 7(6): 949–957. doi:10.1007/s11548-012-0750-1.

## Preclinical evaluation of an MRI-compatible pneumatic robot for angulated needle placement in transperineal prostate interventions

Junichi Tokuda<sup>1</sup>, Sang-Eun Song<sup>1</sup>, Gregory S. Fischer<sup>2</sup>, Iulian Iordachita<sup>3</sup>, Reza Seifabadi<sup>4</sup>, Bong Joon Cho<sup>3</sup>, Kemal Tuncali<sup>1</sup>, Gabor Fichtinger<sup>4</sup>, Clare M. Tempany<sup>1</sup>, and Nobuhiko Hata<sup>1</sup>

<sup>1</sup>Department of Radiology, Brigham and Women's Hospital, Harvard Medical School, 75 Francis St., Boston, MA 02115, USA

<sup>2</sup>Worcester Polytechnic Institute, 100 Institute Road, Worcester, MA 01609, USA

<sup>3</sup>Johns Hopkins University, 3400 North Charles St., Baltimore, MD 21218, USA

<sup>4</sup>School of Computing, Queen's University, 25 Union St., 557 Goodwin Hall, Kingston, ON, K7L 3N6, Canada

### Abstract

**Purpose**—To evaluate the targeting accuracy of a small profile MRI-compatible pneumatic robot for needle placement that can angulate a needle insertion path into a large accessible target volume.

**Methods**—We extended our MRI-compatible pneumatic robot for needle placement to utilize its four degrees-of-freedom (4-DOF) mechanism with two parallel triangular structures and support transperineal prostate biopsies in a closed-bore magnetic resonance imaging (MRI) scanner. The robot is designed to guide a needle towards a lesion so that a radiologist can manually insert it in the bore. The robot is integrated with navigation software that allows an operator to plan angulated needle insertion by selecting a target and an entry point. The targeting error was evaluated while the angle between the needle insertion path and the static magnetic field was between  $-5.7^\circ$  and  $5.7^\circ$  horizontally and between  $-5.7^\circ$  and  $4.3^\circ$  vertically in the MRI scanner after sterilizing and draping the device.

**Results**—The robot positioned the needle for angulated insertion as specified on the navigation software with overall targeting error of  $0.8 \pm 0.5$  mm along the horizontal axis and  $0.8 \pm 0.8$  mm along the vertical axis. The two-dimensional root-mean-square targeting error on the axial slices as containing the targets was 1.4 mm.

**Conclusions**—Our preclinical evaluation demonstrated that the MRI-compatible pneumatic robot for needle placement with the capability to angulate the needle insertion path provides targeting accuracy feasible for clinical MRI-guided prostate interventions. The clinical feasibility has to be established in a clinical study.

### Keywords

MRI-guided therapy; medical robotics; prostate cancer; biopsy; brachytherapy

## Introduction

Magnetic resonance imaging (MRI)-guided prostate biopsy and brachytherapy are active areas of research [1-16], reflecting a strong demand for the precise and minimally-invasive care of prostate cancer. It is the most common cancer among men in the United States [17]. Although transrectal ultrasound (TRUS) [18,19] is the current standard modality for guiding biopsy and brachytherapy, MRI is ideal due to its excellent visualization of the prostate gland, focal lesions, and surrounding periprostatic tissues. MRI is particularly useful if combined with a transperineal approach because it provides better access to the anterior and apical regions of the prostate [20] and can be applied to patients who cannot undergo TRUS-guided biopsy due to previous total colectomy. Given that the MRI-guided approach includes angulated needle paths it can avoid pubic arch interference; thus, it also offers the ability to treat large volume glands that are too large for TRUS-guided procedures. Researchers have been continuously demonstrating the clinical feasibility of transperineal prostate biopsy and brachytherapy guided by intraprocedural MRI [1,2,5,14,13].

One of the major challenges in MRI-guided transperineal prostate interventions is performing procedures in the in-bore space of an MRI scanner and taking full advantage of the intraprocedural imaging to precisely guide a needle to the target. Unfortunately, a conventional 60-cm closed-bore MRI scanner does not allow keeping the patient in the lithotomy position with the legs widely open for easy access to the perineum. Therefore, the patient table is repeatedly withdrawn from the scanner bore: inside for imaging and outside for needle placement, unless a wide-bore MRI scanner is used [16,21]. This precludes the ability to monitor the needle insertion process using real-time MRI, which is becoming available in modern MRI scanners [21-23]. To assist transperineal procedures in the bore, several groups have developed MRI-compatible robotic devices to numerically guide a needle into the prostate. This idea was first demonstrated in an open-configuration MRI scanner [24,25] and then adapted to closed-bore MRI systems [26-28]. These robotic devices, however, do not secure a workspace for a physician to safely access the perineum. Even for robots equipped with needle insertion and tissue sampling or seed deployment mechanisms for a fully automated process, it is crucial to secure safe access to the patient in the bore. To address these issues, we have been developing an MRI-compatible pneumatic robot for needle placement with a four degrees-of-freedom (4-DOF) parallel kinematic structure that effectively utilizes the space under the legs of the patient in the lithotomy position [29,30]. The robot is designed to guide a needle towards a lesion so that a radiologist can manually insert it in the bore. The parallel kinematic structure can position a needle in parallel to the static magnetic field as well as with angulation from the field. While most targets in the prostate can be reached without angulation as practiced in conventional transperineal interventions with needle-guiding templates, some targets require angulated needle placement because of obstacles, e.g. the pubic arch. Those targets cannot be reached by using needle-guiding templates, because they only guide the needle in parallel to the MRI scanner's  $B_0$  field. In spite of its small profile, the robot has kinematics that achieve a range that sufficiently covers the entire prostate gland of most patients by providing the capability to angulate the direction of needle insertion with respect to the static magnetic field.

In this study, we extended the user interface of our robot to allow a physician to plan angulated needle insertions by fully utilizing our unique 4-DOF parallel kinematic structure. Although the kinematic structure was designed for an angulated insertion, it has never been validated with an MRI scanner in our past studies [30,29,31] due to the lack of a practical user interface to plan an angulated needle insertion intuitively. The user interface was integrated with our navigation software, 3D Slicer with ProstateNav software plug-in module, which has been used in our ongoing clinical trial of MRI-guided manual prostate biopsy using a template [23]. We performed a preclinical evaluation of the robot in the same

setting as a clinical procedure, including sterilization and draping, and examined if the robot could achieve the targeting accuracy required for transperineal prostate biopsy [9].

## Materials and Methods

### Pneumatic Robot with 4-DOF Parallel Kinematic Structure

Fig. 1 shows the overview and configuration of the robot with the 4-DOF parallel kinematic structure. The robot has two parallel triangular planar positioning mechanisms parallel to the axial plane of the scanner: one positioned at the front of the robot (front triangular mechanism), facing the perineum, and the second on the feet side of the robot (back triangular mechanism). Those triangular mechanisms are connected by a linkage, which functions as a needle insertion platform. Four pneumatic linear actuators are placed in parallel to the static magnetic field under the kinematic structure to drive the front and the back triangular mechanisms independently. The linear actuation is transmitted to the in-plane positioning of the front and back triangular mechanisms using timing belts. Subsequently, mechanically connecting the summit of the triangular mechanisms (ball joint connections) creates the needle insertion axis, resulting in a 4-DOF angle guide (needle insertion and rotation about its axis are not actuated). The pneumatic linear actuators can be physically locked by brake mechanisms to prevent the robot from accidentally moving during the needle insertion process due to human, software, or electrical errors.

Most of the robot's components are constructed of fully MRI-compatible plastic, with a minimal amount of nonferrous metal including brass (alloy 260 and 360) and anodized aluminum (alloy 6061) to avoid eddy currents and deterioration of magnetic field homogeneity. The linear motion of four pneumatic linear actuators is transmitted to the two triangular mechanisms for planer motion via timing belts (MXL type, trapezoidal teeth, urethane body, Kevlar core, 1/8" width, 0.08" pitch) and pulleys (MXL type, 1/8" width, 0.08" pitch, aluminum body, brass setscrew). Ultem and cast acrylic are used for most of the robot structure and some parts are fabricated from commercial Stereolithography Apparatus (SLA) rapid-prototype service using Acura® 60 plastic (Acu-Cast Technologies, LLC, Lawrenceburg, TN). Optical encoders with shielded differential signals (EM1-0-500-I, US Digital, Vancouver, WA) are used to sense the pneumatic actuator positions.

### System Configuration

The system consists of the following primary components (Fig. 2): 1) the robot with in-room robot controller for low-level servo control; 2) navigation workstation that allows physician and operator to visualize the anatomy and robot workspace and to define targets and entry points for needle placement on MRI images transferred from the scanner; 3) 3 Tesla MRI scanner (MAGNETOM Verio, Siemens Healthcare, Erlangen, Germany). The robot controller is equipped with a computer running Linux-based real-time operating system (RTLinux, Wind River Systems, CA), four pairs of piezoelectric pressure regulator valves to control each of the four pneumatic actuators, and a fiber-optic Ethernet interface enclosed in an EMI-shielded Faraday cage. The controller is connected to the medical air supply connector on the wall of the scanner room to pneumatically drive the robot. Electric power is supplied through a grounded and filtered patch panel on the wall of the scanner room. Thus, the controller can be operated inside the scanner room, approximately 3 m from the isocenter of the MRI scanner without interfering with imaging, while communicating with the navigation workstation located outside the scanner room [27] during image acquisition. The navigation workstation is a Linux-based workstation running open-source medical image computing and visualization software, 3D Slicer [32]. The 3D Slicer software incorporates a plug-in module that adds functionalities to plan targets on an intraprocedural MRI, registers the robot to an image coordinate system using a specially-designed fiducial

marker [22], and sends the coordinates of the planned target to the robot controller through a network using the OpenIGTLink protocol [33]. The navigation workstation also runs a Digital Imaging and Communication in Medicine (DICOM) listener (DCMTK, <http://dicom.offis.de/>) to receive intraprocedural MRI from the host computer of the MRI scanner through the network. The robot controller and the navigation workstation are connected via the fiber-optic network, while the navigation workstation and the host computer of the MRI scanner are connected via 1000-Base T Ethernet.

### User Interface for Needle Insertion Path Planning

Fig. 3 shows the graphical user interface used to define a needle insertion path on the navigation software. The interface provides two methods to specify needle insertion paths: 1) “parallel insertion”, which is parallel to the static magnetic field, by specifying a target point in the prostate on an intraprocedural MRI; 2) “angulated insertion”, by specifying a needle insertion point on the perineum and a target point to define the intended insertion angle. The navigation software calculates the orientation of the needle insertion based on the two points specified and sends it to the controller in a quaternion. Before actual robot operation, the software also overlays 3D models representing a volume reachable by the needle tip onto the images to confirm that the target and the needle insertion angle are within the range of motion of the robot. This feature will allow the physician and operator to decide whether to reposition the robot or the patient before starting the procedure.

### Targeting Experiment

Targeting accuracy of the angulated insertion was evaluated in the 3T MRI scanner as follows:

**Table Setup**—We placed a prostate intervention tabletop setup with built-in leg supports that allows the subject to be positioned in feet-first lithotomy position in the scanner. The tabletop setup has been used in our ongoing clinical trial of MRI-guided prostate biopsy [16,21]. The tabletop consists of a baseboard, leg holders, and attachments to fix the robot and a Z-frame fiducial marker [22,23]. The baseboard is made of a cotton-resin plate designed to fit on the patient table of the MRI scanner. The leg holders, attached to the baseboard by an adjustable attachment, keep the legs apart and raised to secure the workspace between the legs. Two saline phantoms in bottle containers were placed on the right and left of a cubical free space with a dimension of approximately  $100 \times 100 \times 100$  mm, the anticipated location of the prostate in a clinical case. The needle can be placed in this cubical free space in this experiment.

**Calibration**—We first registered the robot to the image coordinate system by localizing the Z-frame fixed to the tabletop as previously described [22,23]. The Z-frame has seven rigid MR visible marker tubes with 7.5 mm inner diameters filled with a contrast agent (MR Spots, Beekley, Bristol, CT) placed on three adjacent faces of a 60 mm cube, thus forming 7 bright spots on an axial image. The navigation software automatically detects the seven rigid tubes on cross-sectional MR images of the Z-frame acquired with the 2D Fast Spin Echo imaging sequence for calibration (TR/TE: 3000/116 ms; acquisition matrix:  $256 \times 256$ ; echo train length: 27; flip angle  $140^\circ$ ; field of view:  $160 \times 160$  mm; slice thickness: 2 mm; receiver bandwidth: 250 Hz/pixel; acquisition time: approx. 1 minute). After localization of the Z-frame, it was replaced by the robot so that the robot was registered to the image coordinate system.

**Robot Setup**—To take any factor that may impact the targeting accuracy into account, we tested the robot in a clinical setting. As shown in Fig. 4, we draped the base of the robot with a sterilized plastic cover designed for use in clinical cases. The base of the robot includes all

but the top ball joints of the front and back triangular mechanisms, which guide the needle, and the top linkage with the needle insertion platform. Sterilization of those parts was validated and certified (Nelson Laboratories, salt Lake City, UT) for the full STERRAD® NX advanced short sterilization cycle to a sterility assurance level (SAL) of  $10^{-6}$  using the biological indicator (BI) overkill method. The sterilized parts were not attached to the robot until the base part of the robot was draped after being placed onto the tabletop.

**Planning**—A multislice planning image of the phantom was acquired using a TSE sequence (TR/TE: 5250/100 ms; acquisition matrix:  $320 \times 224$ ; echo train length: 20; flip angle  $150^\circ$ ; field of view:  $140 \times 140$  mm; slice thickness: 3 mm; receiver bandwidth: 203 Hz/pixel) that has been used for intraoperative imaging in our ongoing clinical trial. The acquired images were transferred to the navigation workstation and loaded into the software. On the planning image, we defined 16 targets in the cubical space; eight were aligned along the vertical axis and eight were aligned along the horizontal axis, as shown by the points in Fig. 3. The targets were placed every 10 mm for the both vertical and horizontal lines. All targets are placed on the same plane to avoid an error variation due to differences in needle insertion depth and to reveal the relationship between the needle placement error and the angulation. The distance between the plane and the Z-frame was 100 mm, which is a typical distance between the Z-frame and targets in the prostate in our ongoing clinical trial of manual MRI-guided prostate biopsy. In addition, one fixed point was defined in the motion range of the back triangular mechanism as a remote center of the needle angulation for evaluation purposes – this point was selected to generate upward insertion paths as would be required to avoid the pubic arch, not as a putative entry point. The distance between the fixed point and the plane that includes the targets was 400 mm. The fixed point was aligned to the cross point of the vertical and horizontal rows of the targets as shown in Fig 3, resulting in angulated insertion with ranges of  $[-5.7^\circ, 5.7^\circ]$  horizontally and  $[-5.7^\circ, 4.3^\circ]$  vertically. The needle insertion paths were calculated based on those points and transferred to the controller, where the inverse kinematics of the robot was computed. The robot moved the needle guide to align with each target position and orientation. In the future clinical applications, the physician and operator will confirm the target and the needle insertion angle are within the range of motion of the robot at this stage and decide whether to reposition the robot or the patient before proceeding to the next step. If the robot needs to be repositioned, the operator will perform the calibration and robot set up steps again.

**Needle Placement**—Before we positioned the robot at each target, we positioned it at a randomly-selected target to take positioning errors due to large robot motion into account. Once the needle insertion path was confirmed on the navigation software, the kinematic structure was physically locked with the brake safety mechanisms. An 18-gauge  $\times$  15-cm MRI-compatible core biopsy needle (MRI Bio Gun, E-Z-EM, Westbury, NY) was manually inserted through the robot's guide sleeve to the needle insertion depth determined by the controller and placed in the cubical free space. The tip of the needle was covered by an MR-visible marker (MR Spots, Beekley, Bristol, CT) to identify the tip of the needle in the cubical free space on confirmation images without inserting the needle into a phantom, which often leads to a needle placement error due to needle deflection. The tip of the needle was identified as a signal void within the marker on the MR images acquired from planes perpendicular to the needle (Fig. 5).

**Validation**—A confirmation image of the needle in the target location was acquired using a multislice TSE sequence (TR/TE: 3000/106 ms; acquisition matrix:  $320 \times 200$ ; echo train length: 27; flip angle  $140^\circ$ ; field of view:  $280 \times 224$  mm; slice thickness: 2 mm; receiver bandwidth: 252 Hz/pixel) after each needle insertion. The center of signal void of the MR-visible marker due to the existence of the needle was identified as the location of the needle



manually on the same slice as the target (Fig. 5). The two-dimensional (2D) needle placement error was evaluated by measuring the distance between the defined target and the center of the needle.

## Results

We could specify the target points with angulation with the newly developed software, achieving a wider range of motion than our previous system, which only allowed parallel insertion. The robotic controller successfully positioned the needle holder with angulated insertion as specified on the navigation software. All needle placements for 16 targets were carried out successfully with target errors less than 3.1 mm. The calibration process was completed instantly without any failure. Fig. 6 shows the relationship between the targeting error and the angle of the needle from the static magnetic field. The overall targeting error was  $0.8 \pm 0.5$  mm along the horizontal X axis and  $0.8 \pm 0.8$  mm along the vertical Y axis. The 2D root-mean-square (RMS) targeting error evaluated on the same axial slices as the targets was 1.4 mm. The total procedure time for 16 targets was 99 minutes, including MR imaging. The time to set up the system and the phantom in the scanner was 31 minutes. The Z-frame image and the planning image were acquired in 6 minutes. The calibration was performed during the acquisition of the planning image. The planning process lasted approximately 5 minutes. The mean duration for targeting, including selection of the target and positioning of the needle, was  $128 \pm 59$  seconds.

## Discussion

In this study, we demonstrated our MRI-compatible needle placement robot with angulated needle placement capabilities and evaluated the targeting accuracy in the MRI scanner. The capability to place a needle with angulated insertion paths is particularly useful when a target in the prostate is not reachable from the perineum with a parallel insertion due to the limited range of target or obstacles between the perineum and the target. Angulated insertion allows the anterior gland to be reached avoiding the pubic arch for large volume glands, for example. The targeting accuracy with angulated insertion was comparable to parallel insertion (1.3 mm) we evaluated in our previous study [31]. Although the study is limited to the evaluations of single oblique (either horizontal or vertical) angulation, we expect the targeting accuracy with a double oblique angulation will be strongly affected by the vertical angulation, because the targeting error was relatively constant for the horizontal angulation. It is also expected that the vertical and horizontal angulations will not affect each other, because they can be decomposed in the difference and the mean displacements of the two linear actuators for the front triangular structure if the back triangular mechanism is fixed as a remote center of rotation.

Targeting errors in prostate biopsies performed with 18-gauge needles in previously published clinical studies were 6.5 mm for a transperineal approach with a needle-guiding template [9] and 5.8 mm for a transrectal approach with a commercially available device [15]. Although we did not take into account deflection of the needle in this study, we expect that the targeting accuracy of 1.4 mm is within an acceptable range for clinical applications, given the targeting accuracies in the existing studies and the contribution of needle deflection evaluated in a previous study using animal tissues, which revealed that the contribution of needle deflection was 0.6 mm for bovine liver and 1.1 mm for bovine muscle tissue at the target 120 mm from the entry point with an 18-gauge symmetrical bevel needle [9]. It should also be noted that the targeting accuracy of 1.4 mm is beyond the theoretical limit for a conventional needle-guide template with a 5 mm interval. The needle placement accuracy we found in this study is comparable to other preclinical studies on image-based evaluation of MRI-compatible robots, which have been used clinically: Schouten et al

achieved needle placement accuracy of 3.0 mm with their pneumatic robot for transrectal biopsy [34]; Krieger et al published their robotic system with hybrid tracking for transrectal biopsy with needle placement accuracy of 1.5 mm [35]; Nuntener et al reported that their MRI-compatible robot for fully-automated transperineal seed placement achieved seed placement accuracy of 0.72 mm [36].

Besides deflection of the needle, there are other factors that may degrade the targeting accuracy of our robot for needle placement. First, air/tissue interfaces near the imaging volume and deoxygenated blood potentially distort the static magnetic field, causing inaccurate localization of targets and the Z-frame; the prostate is adjacent to the rectal wall and also close to the perineum; the Z-frame is placed in a narrow free-space surrounded by the thighs and the perineum of the patients. However, it is still important to validate such an effect with a human subject. Second, shrinkage of the plastic mechanical parts due to repeated sterilization may lead to mechanical inaccuracy. It is important to select a sterilization method that has a minimum impact on the robot's material and to evaluate it thoroughly with the device before clinical application. Our recent work has shown that the selected sterilization method did not affect the needle positioning accuracy in a laboratory setting [37]. Third, the targets cannot be assumed to stay at the same position throughout, because the patient moves during the procedure. The positions of the targets have to be updated. This could be achieved by registering the initial planning image and the images acquired for verification of needle placement. Such an imaging protocol is clinically feasible: our previous report on a clinical trial of manual MRI-guided prostate biopsy with a needle-guiding template demonstrated that a multi-slice turbo spin echo image of the prostate can be acquired after each needle insertion without noticeable image distortion caused by the location of the needle. This image can be used for evaluation of error between the designated target position and the actual needle position [21].

We found one unanticipated issue with angulated insertion that we had not encountered in our previous studies: a larger needle insertion angle was associated with a larger targeting error in the vertical direction. This can be explained by the nature of our triangular kinematics: the ratio of vertical displacement of the triangular mechanism to the displacement of the pneumatic linear actuator is larger at the lower range than the higher range; therefore, a larger error can be observed at the lower position if the back triangular mechanism is fixed. Furthermore, if the front and back triangular mechanisms are positioned independently to angulate the needle, the overall error in the front or back triangular mechanism is geometrically scaled up at the tip of the needle. Because the relationship between displacement of the actuator/encoder and the tip of the triangular mechanism is not linear, calibration of the encoder at the zero position of the triangular mechanism is critical. Further testing is required to tune the kinematic software to improve the calibration accuracy. We also found that the use of drape with the device in the preclinical evaluation is crucial to identify any possible problems in the clinical workflow before a clinical trial. We experienced a reduction in the range of needle placement due to insufficient slack of the drape during our rehearsal session before the experiment. If the drape is not properly attached, it might be trapped by the mechanism, impeding normal operation.

Pubic arch interference has been a major technical limitation during transperineal prostate interventions, especially for the anterior and lateral portion of the prostate. Although we only evaluated needle angulations of approximately  $\pm 5^\circ$  by fixing the back triangular mechanism, the robot can achieve angulation of more than  $10^\circ$  upward by lowering the back triangular mechanism. Needle angulation of  $10^\circ$  would dramatically reduce pubic arch interface; Tincher *et al.* reported that the mean maximum interferences in patients in lithotomy position with 0 and  $20^\circ$  needle angulations were 7.8 and 1.0 mm respectively [38]. Because of the linear trend between targeting error and angulation shown in Figure 6, we

expect that the targeting accuracy at the maximum angulation would still be the same level as manual needle placement with template [9].

There are a number of MRI-compatible actuator technologies, such as pneumatic stepping motors [39,40], air motors [41], ultrasonic motors [42], and piezoelectric motors [43] for MRI-compatible devices. We chose the pneumatic cylinders to drive our parallel triangular mechanism to achieve the low-profile kinematic structure that allows the radiologist to manually insert a needle into the patient at the imaging position. Securing in-bore workspace for the radiologist is particularly important for the smooth transition from the manual procedure to the robotic procedure, and for patient safety.

In conclusion, our preclinical evaluation demonstrated that the MRI-compatible pneumatic robot for needle placement with 4-DOF parallel kinematic structure provides better targeting accuracy than the theoretical limit of conventional manual needle-guiding templates even with angulated needle insertion path suggesting that this robotic device can be used in clinical practice. The clinical feasibility has to be established in a clinical study.

## Acknowledgments

This work is supported by National Institute of Health Grants R01CA111288, P01CA067165, R01CA124377, P41RR019703, P41EB015898, R01CA138586, and CIMIT 11-325.

## References

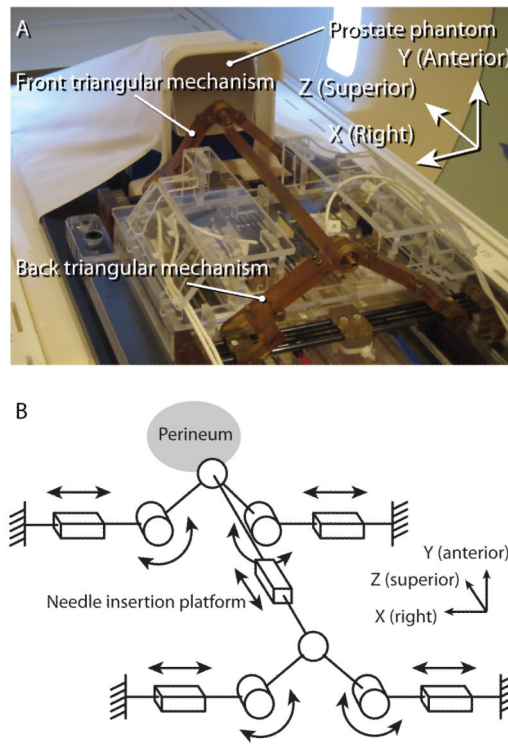
1. Cormack RA, D'Amico AV, Hata N, Silverman S, Weinstein M, Tempany CM. Feasibility of transperineal prostate biopsy under interventional magnetic resonance guidance. *Urology*. 2000; 56(4):663–664. doi:S0090-4295(00)00698-1 [pii]. [PubMed: 11018628]
2. D'Amico AV, Tempany CM, Cormack R, Hata N, Jinzaki M, Tuncali K, Weinstein M, Richie JP. Transperineal magnetic resonance image guided prostate biopsy. *J Urol*. 2000; 164(2):385–387. doi:S0022-5347(05)67366-1 [pii]. [PubMed: 10893591]
3. Susil RC, Krieger A, Derbyshire JA, Tanacs A, Whitcomb LL, Fichtinger G, Atalar E. System for MR image-guided prostate interventions: canine study. *Radiology*. 2003; 228(3):886–894. doi: 10.1148/radiol.2283020911 228/3/886 [pii]. [PubMed: 12954903]
4. Menard C, Susil RC, Choyke P, Gustafson GS, Kammerer W, Ning H, Miller RW, Ullman KL, Sears Crouse N, Smith S, Lessard E, Pouliot J, Wright V, McVeigh E, Coleman CN, Camphausen K. MRI-guided HDR prostate brachytherapy in standard 1.5T scanner. *Int J Radiat Oncol Biol Phys*. 2004; 59(5):1414–1423. doi:10.1016/j.ijrobp.2004.01.016 S036030160400118X [pii]. [PubMed: 15275727]
5. Susil RC, Camphausen K, Choyke P, McVeigh ER, Gustafson GS, Ning H, Miller RW, Atalar E, Coleman CN, Menard C. System for prostate brachytherapy and biopsy in a standard 1. T MRI scanner. *Magn Reson Med*. 2004; 52(3):683–687. doi:10.1002/mrm.20138.
6. Zangos S, Eichler K, Engelmann K, Ahmed M, Dettmer S, Herzog C, Pegios W, Wetter A, Lehnert T, Mack MG, Vogl TJ. MR-guided transgluteal biopsies with an open low-field system in patients with clinically suspected prostate cancer: technique and preliminary results. *Eur Radiol*. 2005; 15(1):174–182. doi:10.1007/s00330-004-2458-2. [PubMed: 15351902]
7. Engelhard K, Hollenbach HP, Kiefer B, Winkel A, Goeb K, Engehausen D. Prostate biopsy in the supine position in a standard 1. T scanner under real time MR-imaging control using a MR-compatible endorectal biopsy device. *Eur Radiol*. 2006; 16(6):1237–1243. doi:10.1007/s00330-005-0100-6.
8. Susil RC, Menard C, Krieger A, Coleman JA, Camphausen K, Choyke P, Fichtinger G, Whitcomb LL, Coleman CN, Atalar E. Transrectal prostate biopsy and fiducial marker placement in a standard 1.5T magnetic resonance imaging scanner. *J Urol*. 2006; 175(1):113–120. doi:S0022-5347(05)00065-0 [pii] 10.1016/S0022-5347(05)00065-0. [PubMed: 16406885]



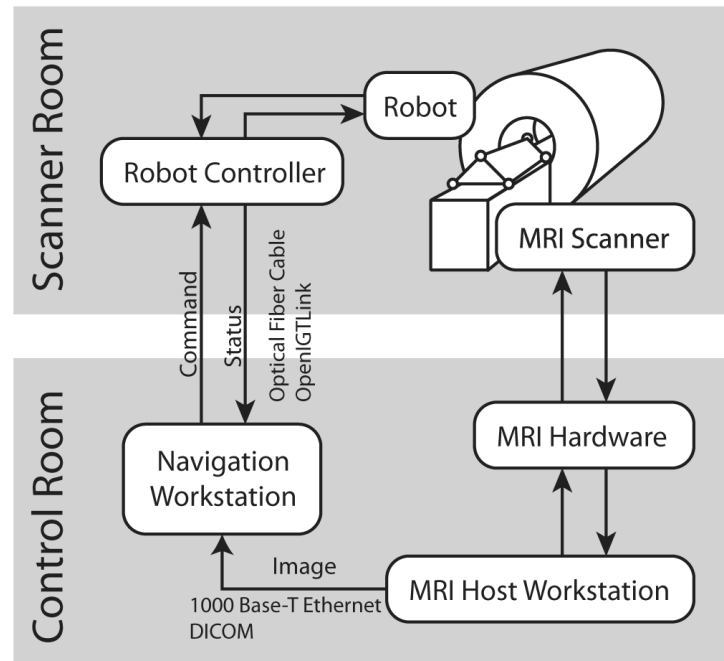
9. Blumenfeld P, Hata N, DiMaio S, Zou K, Haker S, Fichtinger G, Tempany CM. Transperineal prostate biopsy under magnetic resonance image guidance: a needle placement accuracy study. *J Magn Reson Imaging*. 2007; 26(3):688–694. doi:10.1002/jmri.21067. [PubMed: 17729363]
10. Hambrock T, Futterer JJ, Huisman HJ, Hulsbergen-vandeKaa C, van Basten JP, van Oort I, Witjes JA, Barentsz JO. Thirty-two-channel coil 3T magnetic resonance-guided biopsies of prostate tumor suspicious regions identified on multimodality 3T magnetic resonance imaging: technique and feasibility. *Invest Radiol*. 2008; 43(10):686–694. doi:10.1097/RLI.0b013e31817d0506 00004424-200810000-00002 [pii]. [PubMed: 18791410]
11. Rea M, McRobbie D, Elhawary H, Tse ZTH, Lamperth M, Young I. System for 3-D Real-Time Tracking of MRI-Compatible Devices by Image Processing. *IEEE-ASME Transactions on Mechatronics*. 2008; 13(3):379–382.
12. Lakosi F, Antal G, Vandulek C, Kovacs A, Garamvolgyi R, Petnehazy O, Bajzik G, Hadjiev J, Repa I, Bogner P. Technical feasibility of transperineal MR-guided prostate interventions in a low-field open MRI unit: canine study. *Pathol Oncol Res*. 2009; 15(3):315–322. doi:10.1007/s12253-008-9111-3. [PubMed: 18946728]
13. Menard, C.; Chung, P.; Abed, J.; Simeonov, A.; Lee, J.; Brock, K.; Foltz, W.; O’Leary, G.; Elliott, C.; Milosevic, M.; Bristow, R.; Morton, G.; Warde, P.; Haider, M. Online Guidance of Tumor Targeted Prostate Brachytherapy using Histologically Referenced MRI. Paper presented at the Proc. Intl. Soc. Mag. Reson. Med.; Stockholm, Sweden. May 1-7, 2010; 2010.
14. Menard, C.; Iupati, D.; Lee, J.; Simeonov, A.; Abed, J.; Publicover, J.; Chung, P.; Bayley, A.; Catton, C.; Milosevic, M.; Bristow, R.; Morton, G.; Warde, P.; Brock, K.; Haider, M. MRI and Biopsy Performance in Delineating Recurrent Tumor Boundaries after Radiotherapy for Prostate Cancer. Paper presented at the Proc. Intl. Soc. Mag. Reson. Med.; Montreal, Quebec, Canada. May 7-13, 2011; 2011.
15. Schouten, MG.; Bomers, JG.; Yakar, D.; Huisman, H.; Scheenen, TW.; Misra, S.; Futterer, JJ. Proc. Intl. Soc. Mag. Reson. Med. Montreal, Quebec, Canada: 2011. Transrectal MRI-guided prostate biopsy: evaluation of a novel robotic technique; p. 1060
16. Tuncali, K.; Tokuda, J.; Fedorov, A.; Iordachita, I.; Song, S.; Oguro, S.; Lasso, A.; Fennessy, FM.; Tang, Y.; Hata, N.; Tempany, CM. 3T MRI-guided Transperineal Targeted Prostate Biopsy: Clinical Feasibility, Safety, and Early Results. Paper presented at the 19th Annual Meeting and Exhibition, International Society of Magnetic Resonance in Medicine; Montreal, Canada. 7-13 May, 2011; 2011.
17. Siegel R, Naishadham D, Jemal A. Cancer statistics, 2012. *CA Cancer J Clin*. 2012; 62(1):10–29. doi:10.3322/caac.20138. [PubMed: 22237781]
18. Hodge KK, McNeal JE, Terris MK, Stamey TA. Random systematic versus directed ultrasound guided transrectal core biopsies of the prostate. *J Urol*. 1989; 142(1):71–74. discussion 74-75. [PubMed: 2659827]
19. Scherr DS, Eastham J, Ohori M, Scardino PT. Prostate biopsy techniques and indications: when, where, and how? *Semin Urol Oncol*. 2002; 20(1):18–31. doi:S1081094302500139 [pii]. [PubMed: 11828354]
20. Sartor AO, Hricak H, Wheeler TM, Coleman J, Penson DF, Carroll PR, Rubin MA, Scardino PT. Evaluating localized prostate cancer and identifying candidates for focal therapy. *Urology*. 2008; 72(6 Suppl):S12–24. doi:S0090-4295(08)01732-9 [pii] 10.1016/j.urology.2008.10.004. [PubMed: 19095124]
21. Tokuda, J.; Tuncali, K.; Iordachita, I.; Song, S.; Fedorov, A.; Oguro, S.; Lasso, A.; Fennessy, F.; Tang, Y.; Tempany, C.; Hata, N. Preliminary Accuracy Evaluation of 3T MRI-guided Transperineal Prostate Biopsy with Grid Template. Paper presented at the 19th Annual Meeting and Exhibition, International Society of Magnetic Resonance in Medicine; Montreal, Canada. 7-13 May, 2011; 2011.
22. DiMaio SP, Samset E, Fischer G, Iordachita I, Fichtinger G, Jolesz F, Tempany CM. Dynamic MRI scan plane control for passive tracking of instruments and devices. *Med Image Comput Comput Assist Interv*. 2007; 10(Pt 2):50–58. [PubMed: 18044552]
23. Tokuda J, Fischer GS, Csoma C, DiMaio SP, Gobbi DG, Fichtinger G, Tempany CM, Hata N. Software strategy for robotic transperineal prostate therapy in closed-bore MRI. *Med Image Comput Comput Assist Interv*. 2008; 11(Pt 2):701–709. [PubMed: 18982666]

24. Chinzei, K.; Hata, N.; Jolesz, F.; Kikinis, R. MR Compatible Surgical Assist Robot: System Integration and Preliminary Feasibility Study. *Medical Image Computing and Computer-Assisted Intervention – MICCAI 2000* 1935. 2000.
25. DiMaio S, Pieper S, Chinzei KH, N, Haker S, Kacher D, Fichtinger G, Tempany C, Kikinis R. Robot-assisted needle placement in open MRI: system architecture, integration and validation. *Comput Aided Surg.* 2007; 12:15–24. [PubMed: 17364655]
26. Patriciu A, Petrisor D, Muntener M, Mazilu D, Schar M, Stoianovici D. Automatic brachytherapy seed placement under MRI guidance. *IEEE Trans Biomed Eng.* 2007; 54:1499–1506. [PubMed: 17694871]
27. Fischer GS, Iordachita I, Csoma C, Tokuda J, DiMaio SP, Tempany CM, Hata N, Fichtinger G. MRI-Compatible Pneumatic Robot for Transperineal Prostate Needle Placement. *IEEE/ASME Trans Mechatronics.* 2008; 13(3):295–305.
28. van den Bosch M, Moman M, van Vulpen M, Battermann J, Duiveman E, van Schelven L, de Leeuw H, Lagendijk J, Moerland M. MRI-guided robotic system for transperineal prostate interventions: proof of principle. *Phys Med Biol.* 2010; 55:N133–140. [PubMed: 20145293]
29. Song SE, Cho N, Tokuda J, Hata N, Tempany C, Fichtinger G, Iordachita I. Preliminary Evaluation of a MRI-compatible Modular Robotic System for MRI-guided Prostate Interventions. *Proc IEEE RAS EMBS Int Conf Biomed Robot Biomechatron.* 2010; 2010:796–801. doi:10.1109/BIOROB.2010.5626987. [PubMed: 21132087]
30. Song SE, Cho NB, Fischer G, Hata N, Tempany C, Fichtinger G, Iordachita I. Development of a Pneumatic Robot for MRI-guided Transperineal Prostate Biopsy and Brachytherapy: New Approaches. *IEEE Int Conf Robot Autom.* 2010; 2010:2580–2585. doi:10.1109/ROBOT.2010.5509710. [PubMed: 21399734]
31. Seifabadi R, Song SE, Krieger A, Cho NB, Tokuda J, Fichtinger G, Iordachita I. Robotic system for MRI-guided prostate biopsy: feasibility of teleoperated needle insertion and ex vivo phantom study. *Int J Comput Assist Radiol Surg.* 2011 doi:10.1007/s11548-011-0598-9.
32. Gering DT, Nabavi A, Kikinis R, Hata N, O'Donnell LJ, Grimson WE, Jolesz FA, Black PM, Wells WM 3rd. An integrated visualization system for surgical planning and guidance using image fusion and an open MR. *J Magn Reson Imaging.* 2001; 13(6):967–975. doi:10.1002/jmri.1139 [pii]. [PubMed: 11382961]
33. Tokuda J, Fischer GS, Papademetris X, Yaniv Z, Ibanez L, Cheng P, Liu H, Blevins J, Arata J, Golby AJ, Kapur T, Pieper S, Burdette EC, Fichtinger G, Tempany CM, Hata N. OpenIGTLink: an open network protocol for image-guided therapy environment. *Int J Med Robot.* 2009; 5(4): 423–434. doi:10.1002/rcs.274. [PubMed: 19621334]
34. Schouten MG, Ansems J, Renema WK, Bosboom D, Scheenen TW, Futterer JJ. The accuracy and safety aspects of a novel robotic needle guide manipulator to perform transrectal prostate biopsies. *Med Phys.* 2010; 37(9):4744–4750. [PubMed: 20964192]
35. Krieger A, Iordachita II, Guion P, Singh AK, Kaushal A, Menard C, Pinto PA, Camphausen K, Fichtinger G, Whitcomb LL. An MRI-compatible robotic system with hybrid tracking for MRI-guided prostate intervention. *IEEE Trans Biomed Eng.* 2011; 58(11):3049–3060. doi:10.1109/TBME.2011.2134096. [PubMed: 22009867]
36. Muntener M, Patriciu A, Petrisor D, Mazilu D, Bagga H, Kavoussi L, Cleary K, Stoianovici D. Magnetic resonance imaging compatible robotic system for fully automated brachytherapy seed placement. *Urology.* 2006; 68(6):1313–1317. doi:S0090-4295(06)02089-9 [pii] 10.1016/j.urology.2006.08.1089. [PubMed: 17169653]
37. Seifabadi R, Cho NB, Song SE, Tokuda J, Hata N, Tempany CM, Fichtinger G, Iordachita I. Accuracy Study of a MRI-guided Robotic System for Prostate Biopsy. *Int J Med Robot.* 2012 (In Press).
38. Tincher SA, Kim RY, Ezekiel MP, Zinsli T, Fiveash JB, Raben DA, Bueschen AJ, Urban DA. Effects of pelvic rotation and needle angle on pubic arch interference during transperineal prostate implants. *Int J Radiat Oncol Biol Phys.* 2000; 47(2):361–363. doi:S0360-3016(00)00434-X [pii]. [PubMed: 10802360]
39. Stoianovici D, Song D, Petrisor D, Ursu D, Mazilu D, Muntener M, Schar M, Patriciu A. “MRI Stealth” robot for prostate interventions. *Minim Invasive Ther Allied Technol.* 2007; 16(4):241–248. doi:780499259 [pii] 10.1080/13645700701520735. [PubMed: 17763098]

40. Elhawary H, Zivanovic A, Rea M, Tse ZT, McRobbie D, Young I, Paley M, Davies B, Lamperth M. A MR compatible mechatronic system to facilitate magic angle experiments in vivo. *Med Image Comput Comput Assist Interv.* 2007; 10(Pt 2):604–611. [PubMed: 18044618]
41. Taillant E, Avila-Vilchis J, Allegrini C, Bricault I, Cinquin P. CT and MR Compatible Light Puncture Robot: Architectural Design and First Experiments. *Med Image Comput Comput Assist Interv.* 2004; 3217:145–152.
42. Suzuki, T.; Liao, H.; Kobayashi, E.; Sakuma, I. Ultrasonic motor driving method for EMI-free image in MR image-guided surgical robotic system. *Proc IEEE/RSJ Int Conf Intelligent Robots and Systems;* 2007. p. 522-527.
43. Elhawary H, Zivanovic A, Rea M, Davies B, Besant C, McRobbie D, de Souza N, Young I, Lamprth M. The Feasibility of MR-Image Guided Prostate Biopsy Using Piezoceramic Motors Inside or Near to the Magnet Isocentre. *Med Image Comput Comput Assist Interv.* 2006; 9(Pt 1): 519–526. [PubMed: 17354930]

**Fig. 1.**

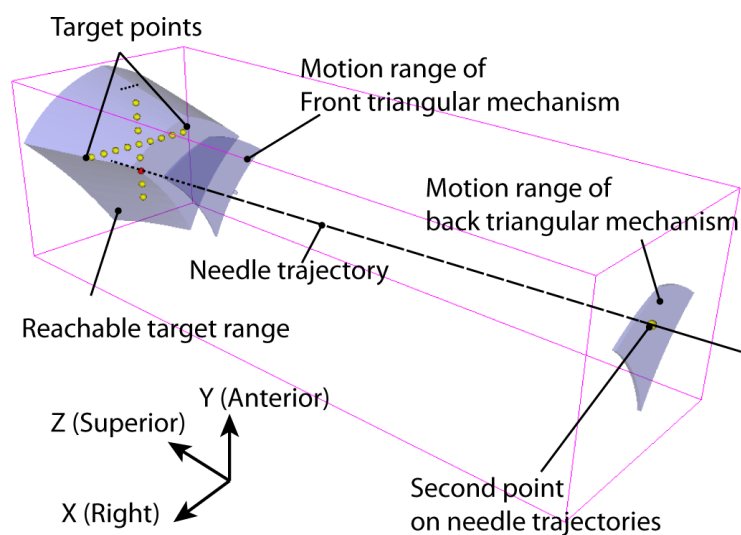
(A) The photo shows an overview of the 4-DOF MRI-compatible pneumatic needle placement robot and the agar phantom placed on the patient table of the MRI scanner. The phantom was removed from the scanner during the needle placement in the experiment. (B) The robot with 4-DOF parallel kinematic structure has two identical triangular planar positioning mechanisms that move within the  $x$ - $y$  plane (axial in patient coordinate system) and are connected by a linkage as a needle insertion platform. The needle is manually inserted into the prostate through the perineum after the robot positions and orients the needle insertion platform.



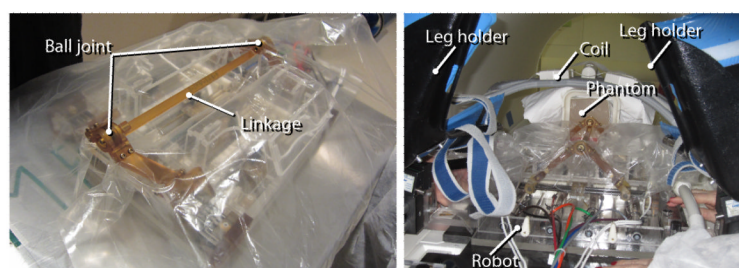
**Fig. 2.**

The configuration of the robot system for MRI-guided prostate interventions. Robot controller for low-level servo control of the robot is placed in the scanner room, while the navigation workstation is placed next to the host workstation of the MRI scanner system in the control room. Optical fiber Ethernet is used for network communication between the robot controller and navigation workstation to shut off electromagnetic (EM) noise from outside the EM shielded scanner room.



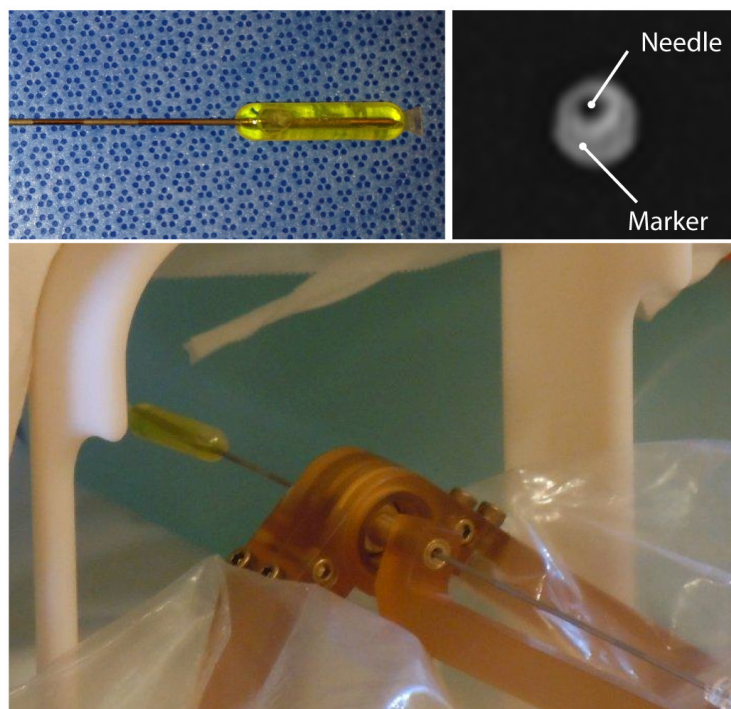


**Fig. 3.**  
The screenshot of the navigation software based on 3D Slicer shows the 3D models representing reachable target range and motion range of the front and back triangular-shaped links.



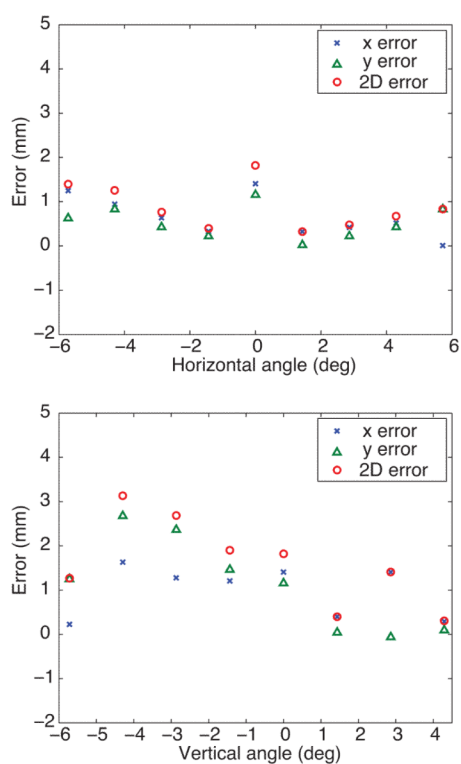
**Fig. 4.**

The robot was draped with a transparent plastic cover for sterilization of the interventional workspace. Only the base of the robot, which is not sterilizable, is draped. The linkage that connects the two triangular mechanisms and the ball joints that hold the needle were sterilized before the procedure and attached to the base part of the robot. The four links of the front and back triangular mechanisms penetrate the cover.



**Fig. 5.**

The tip of the needle was covered by an MRI-visible marker (upper left) so that the tip of the needle can be identified as an artifact on an MR image acquired from a plane perpendicular to the needle (upper right). The bottom photo shows the needle with the marker placed at the target by the robot.

**Fig. 6.**

The plots show the error of needle placement in the  $x$ -axis (horizontal: right-left axis of the patient) and  $y$ -axis (vertical: anterior-posterior axis of the patient) with respect to the needle angle from the static field.